Composites Science and Technology 186 (2020) 107935

Contents lists available at ScienceDirect

Composites Science and Technology

journal homepage: http://www.elsevier.com/locate/compscitech

4D printed anisotropic structures with tailored mechanical behaviors and shape memory effects

Tianzhen Liu [a], Liwu Liu [b], Chengjun Zeng [b], Yanju Liu [b], Jinsong Leng [a,*]

[a] National Key Laboratory of Science and Technology on Advanced Composite in Special Environments, Harbin Institute of Technology, Harbin, 150080, PR China
[b] Department of Astronautical Science and Mechanics, Harbin Institute of Technology (HIT), No. 92 West Dazhi Street, PO Box 301, Harbin, 150001, PR China

ARTICLE INFO

Keywords:
4D printing
Shape memory behavior
Infill pattern
Mechanical property
Anisotropy

ABSTRACT

Four-dimensional (4D) printing as a new generation additive manufacturing of smart materials has shown great potential for the intelligent development of multi-functional and customized structures. The microarchitecture design of printing infill patterns could bring flexible and diversified structural performances by combining the geometry design, thus opening up more possibilities for practical application. This work investigates the anisotropic characteristics of mechanical and shape memory performances induced by different infill strategies via both experimental and theoretical methods. Uniaxial tensile tests and compressive tests are performed to study the effect of infill patterns on mechanical properties. Both classical laminate plate theory and honeycomb equivalent modulus theory take into account the actual shape and dimensions of printed cross-section to improve the prediction accuracy. The viscoelasticity of each printing pattern is described by generalized Maxwell-Wiechert model and Prony Series are fitted to provide references to implement in Abaqus. With the purpose of exploring the shape memory properties including recovery speed, recovery ratio and shape fixity ratio, deformation-recovery tests are conducted under different temperatures and a 2D and 3D convertible structure with programmable Poisson's ratio are demonstrated. This work may potentially provide pattern design guidance for 4D printing structures to meet different application requirements.

1. Introduction

Many structures in nature have evolved to be anisotropic for the adaption of different functional requirements [1] in different directions, such as biological tissues [2] and crystals [3]. People have also developed various anisotropic structures to design the load path inspired by nature [4–6], thus further tuning the mechanical properties directionally and optimizing the performance. Recently, the rapid development of three-dimensional (3D) printing technique provides more opportunity and possibility for the fabrication of complex structures and achieving multifunctionality [7–12] due to the advantages of single step manufacture, low cost, design freedom and customization [13–16]. Tibbits first presented the concept of four-dimensional (4D) printing structures in 2013 [17], which have the capability to transform from one state to another over time independently under specific environments or certain stimuli. 4D printing is the further development of 3D printing adding the time dimension on the basis of static structures [14,18–20]. Specifically, 4D printing makes it possible to fabricate complex three-dimensional objects that are smart and can achieve the transformation of structures and functions by the combination of 3D printing technology and smart materials [21–23]. It's well known that shape memory polymer (SMP) is a kind of smart material that is able to respond to external stimuli [24,25], such as heating [26,27], light exposure [28], magnetic fields [29], electrical current [30] and water immersion [31] and deform from a temporary shape to the original shape. In order to change the configuration or function in response to an environmental stimulus, one can activate the active material subsequently in a controlled manner. A great upsurge of research on 4D printing SMP has been coming in both academia and industry [32,33], providing more development space for 4D printing and SMP in high-tech fields, such as smart implants [34], flexible electronics [35,36], and biomedical sensing [37].

It has been found that various printing parameters including fill density, printing temperature, layer thickness and build direction have a significant influence on the mechanical performance of printed structures [38,39]. Gautam et al. investigated the influence of truss radius, surface roughness and building orientation on strength and stiffness and found that compressive properties could be improved by reducing the roughness with surface treatment [40]. Yin et al. demonstrated that the

* Corresponding author.
E-mail address: lengjs@hit.edu.cn (J. Leng).

https://doi.org/10.1016/j.compscitech.2019.107935
Received 28 May 2019; Received in revised form 5 November 2019; Accepted 21 November 2019
Available online 25 November 2019

interfacial bonding strength of polyurethane (TPU)/acrylonitrile butadiene styrene (ABS) bi-material structures could be enhanced significantly by the increase of building stage temperature [41]. Huneault et al. explored the mechanical properties of cellular printed Polylactic acid (PLA) under uniaxial tensile loading and 3-point bending tests [42]. Different printing infill patterns could bring structural anisotropy [43] in the aspect of elasticity, viscoelasticity and shape memory effect, which have been given very little attention so far. Previous studies have primarily focused on characterizing and optimizing printing parameters for fully dense PLA structures. Note that the infill patterns discussed in this paper refer to how printed filaments fill every position of the desired structure, which differ from the case that the desired structure itself is cellular or has some other patterns. It's possible to design the patterns that filaments adopted to infill printed regions to be straight line or polygon with different angles to obtain targeted properties, which highlights the need for a better understanding of the influence of infill strategies on the anisotropy and performance of structures.

Besides the experimental studies, it's necessary to develop predictive models to offer guidance for the design of mechanical properties. However, few papers in literature report theoretical research to provide predictive models to determine the mechanical properties of printed structures [44], especially the comparison between experimental and theoretical results. Casavola et al. investigated the mechanical behaviors of printed samples using classical laminate theory with one stack sequence validity verification [44]. Croccolo et al. considered some printing parameters and built an analytical model to predict the mechanical properties, for which adhesive forces needed to be introduced [45]. More work focused on theoretical prediction of the mechanical properties is in demand.

The purpose of this work is to systematically study the anisotropic characteristics of mechanical and shape memory performances via both experimental and theoretical methods, which fills the above-mentioned gap in literature. It turns out that the mechanical property and shape memory effect can be highly dependent on the microstructures. The mechanical properties of single printed layer are measured with specimens of straight line $[0]_{10}$, $[90]_{10}$ and $[\pm45]_5$ under uniaxial tension to calculate the parameters of multi-layer structures $[\pm60]_5$ and $[0/90]_5$ through the classical laminate theory, which then are compared with experimental data to verify the validity of the equivalent method. Here the number in square brackets represents the printing direction, while the subscripts represent the number of layers. The tensile and compressive performances of polygon filled pattern specimens are evaluated by honeycomb equivalent modulus theory and mechanical tests. Classical laminate theory and honeycomb equivalent modulus theory are modified to predict the parameters of straight-line and polygonal patterns, respectively. Generalized Maxwell-Wiechert model is applied to describe the viscoelasticity of each printing pattern and Prony Series are fitted through relaxation tests to provide references to implement in Abaqus. Finally, deformation-recovery tests and a demonstration of a 2D and 3D convertible structure with programmable Poisson's ratio are conducted to study the shape memory properties.

2. Experiments

2.1. Printing pattern design and FDM processing conditions

In this study, the materials employed to fabricate 4D printed structures were shape memory PLA filaments developed by Jinsong Leng's group [46]. The thermal properties of filaments have been studied systematically using differential scanning calorimetry (DSC) and thermal gravimetric analysis (TGA) measurements [46], from which it can be seen that the glass transition temperature (Tg), crystallization temperature, melting temperature and degradation temperature were about 63 °C, 110 °C, 170°Cand 345 °C, respectively. The 4D printing technique was fused deposition modeling (FDM), which could squeeze printed material from the nozzle by heating and pile up layers to 3D structure, mainly aiming at thermoplastic material and its composite. An open 4D printer was adopted, which allowed to change printed path to obtain designed layer filling pattern. Here, in order to investigate the influence of printed path on structural mechanical properties, three types of filling strategies including straight line, triangle and hexagon were developed, among which straight line corresponds to five kinds of path directions ([0], [90], [±45], [0/90], [±60]), triangle and hexagon both correspond to two kinds of path directions ([0], [90]). The thickness of each specimen is 2 mm with 10 printed layers. The total nine combinations of filling strategies and path directions are demonstrated in Fig. 1. Other key printing parameters are listed in Table 1 according to the thermal properties of PLA filaments. Considering the scale of the filling patterns, optical microscopy was used to observe the morphologies of both cross section and in-plane surfaces, conducted on a KEYENCE VHX-900 microscope.

2.2. Mechanical experiments

2.2.1. Uniaxial tensile tests

Tensile experiments were conducted using INSTRON 3344 with a constant loading rate 2 mm/min in order to explore the anisotropy of specimens with different printing patterns. Specifically, the straight-line patterns with [0], [90] and [±45] were used for the measurement of single layer parameters, including the modulus E_1, E_2, and Poisson's ratio ν_{12},ν_{21}. The patterns of triangle, hexagon and straight line with [0/90], [±60] were tested to verify the validity of equivalent theory by comparing the theoretical and experimental results. The filaments alone with effective length of 165 mm were stretched to obtain the modulus E_m of shape memory PLA. The strain and displacement distributions during the tension process were investigated through digital image correlation (DIC) technique. Two cameras adopted possess resolution of 2448 × 2048 pixels and lens of 25 mm, collecting changing surface images at a frequency of 5 Hz. The specimens (three of each printing pattern) tested were sprayed with white background and black speckles for the purpose of improving contrast shown in Fig. 2a.

2.2.2. Compression tests

In addition to the tensile properties, the printing patterns serving as internal 'microstructures' are also able to affect the stress-strain relationship and fracture morphology under compressive condition in practical application. INSTRON 5569 was adopted to perform the compression tests on the specimens with filling paths of triangle and hexagon, both of which were tested in two directions of 0°and 90°to demonstrate the anisotropic properties. The fracture morphologies before and after compression were observed through a KEYENCE VHX-900 microscope.

2.2.3. Relaxation experiments

It's well-known that SMPs show obvious viscoelastic characteristics especially in the vicinity of Tg, which plays a significant role in the long-term service. 4D printed structures with different infill patterns could potentially influence the relaxation behavior by guiding the load path at constant strain. Stress relaxation tests were performed at 65 °C using ZWICK/Z010 on printed specimens (straight line $[0]_{10}$, $[90]_{10}$, $[0/90]_5$, hexagon $[0]_{10}$, $[90]_{10}$ and triangle $[0]_{10}$, $[90]_{10}$). Specimens were maintained at 65 °C for 10 min to reach the temperature equilibrium at stress free state, followed by the loading process with the strain rate of 0.1/s and relaxation step for 20 min under the strain of 10%.

2.3. Shape memory recovery tests

In order to investigate the effects of structural anisotropy brought by different printing patterns on shape memory recovery properties, some evaluations on the characters of shape memory polymer were studied experimentally, such as the shape retention and recovery ratio, and shape recovery speed under different temperatures. Nine kinds of

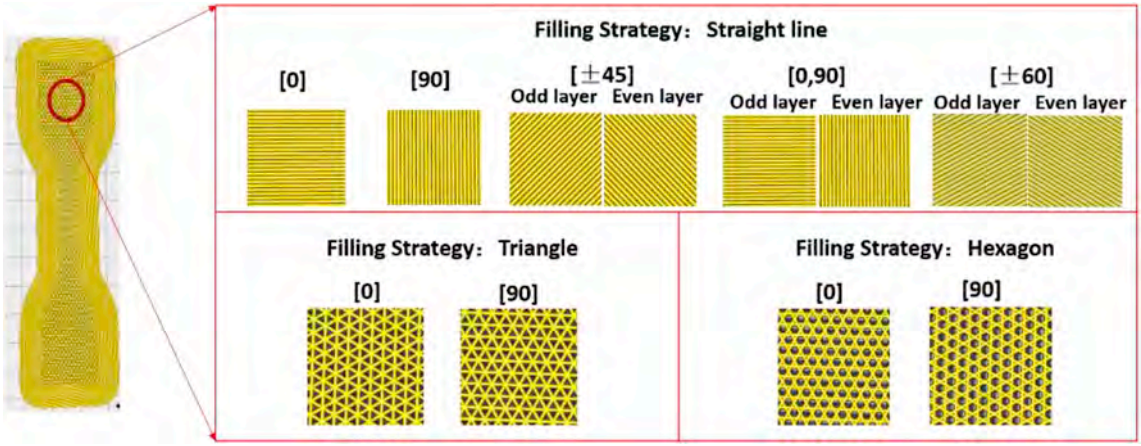

Fig. 1. Filling strategies of printed shape memory PLA.

Table 1
Printing parameters.

Type	Value
Layer height	0.2 mm
Bottom thickness	0.3 mm
Fill density	99%
Fill pattern	straight line/triangle/hexagon
Path direction	[0], [90], [0,90], [±45], [±60]
Printing Temperature	185 °C
Bed temperature	20 °C
Filament diameter	1.5 mm
Flow	100%
Print speed	40 mm/s
Platform adhesion type	Brim

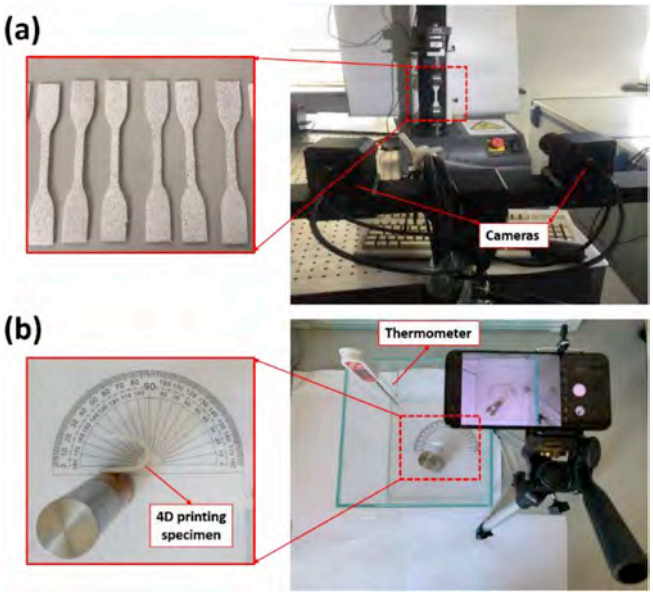

Fig. 2. Experimental setups (a) Tension experiment setup and specimens sprayed with white background and black speckles. (b) Shape memory recovery test setup.

specimens in Fig. 1 with dimension of 15*80*2 mm were pre-programmed to U type under glass transition temperature. The shape recovery ratio and speed tests were conducted in hot water under the temperature in the vicinity of Tg, which were 55 °C, 60 °C and 65 °C. A protractor was attached on the bottom of water container and a thermometer in the water was to monitor the temperature shown in Fig. 2b. For shape retention ratio, the U type specimens were placed on smooth surface at room temperature for 20 h, during which the recovery angles were recorded at the time points of 1 min, 2 min, 3 min, 4 min, 5 min, 10 min, 20 min, 30 min, 40 min, 50 min, 100 min, 200 min, 500 min, 1200 min.

3. Prediction of effective parameters for different filling strategies

The cellular filling patterns bring internal 'microstructures' for macroscopic printed structures, leading to anisotropic mechanical performances. It's necessary to predict the effective properties to provide guidance for design and application. The predictive models in this paper offer general approaches to analyze the deformation behaviors for most printed structural parts with high printing density. Proper modification should be made when applying to low-density structures.

3.1. Filling strategy: straight line

A single layer with the pattern of straight line exhibits obvious mechanical anisotropy along the printed direction and the perpendicular direction. The adhesive strength between printed filaments is lower than that along the printed direction, the mutual functions of which are similar to fiber and matrix in uni-directional composite plies. Based on this assumption, classical laminate theory was adopted and modified for 3D printed structures with the pattern of straight line in this paper, as demonstrated in the Supplementary Information (SI) section S1. Single layer parameters, including the modulus E_1, E_2, and Poisson's ratio ν_{12}, ν_{21} are measured and calculated using straight-line patterns with [0], [90] and [±45] in Supplementary Information (SI) section S2.

3.1.1. Calculation and analyzation of material parameters in different printing paths

To verify the validity of the equivalent theory, the equivalent modulus of two types of printed structures $[0/90]_5$ and $[\pm 60]_5$ were calculated in order to compare with experimental results. $[0/90]_5$ and $[\pm 60]_5$ belong to cross-ply and antisymmetric multilayer printed structures, respectively.

3.1.1.1. Printing pattern $[0/90]_5$. The relationship between force and strain for $[0/90]_5$ can be written as

$$\begin{bmatrix} N_x \\ N_y \\ N_{xy} \end{bmatrix} = \begin{bmatrix} A_{11} & A_{12} & 0 \\ A_{12} & A_{11} & 0 \\ 0 & 0 & A_{66} \end{bmatrix} \begin{bmatrix} \varepsilon_x^0 \\ \varepsilon_y^0 \\ \gamma_{xy}^0 \end{bmatrix} + \begin{bmatrix} B_{11} & 0 & 0 \\ 0 & -B_{11} & 0 \\ 0 & 0 & 0 \end{bmatrix} \begin{bmatrix} K_x \\ K_y \\ K_{xy} \end{bmatrix} \quad (1)$$

where $A_{11} = A_{22} = 5t_0(Q_{11} + Q_{22}), A_{12} = 10t_0Q_{12}, A_{66} = 10t_0Q_{66}$.

Since the thickness is relatively small, when compared with the other two dimensions, here the coupling between tension and bending deformation is neglected, which leads to $\mathbf{B} = 0$.

Substituting Eq.(S1) into the components of matrix A and Eq.(S9), the equivalent modulus is expressed as

$$E_{[0/90]x} = E_{[0/90]y} = \frac{(E_1 + E_2)^2 - 4(v_{12}E_1)^2}{2(E_1 + E_2)(1 - v_{12}v_{21})} \tag{2}$$

3.1.1.2. Printing pattern [±60]5. Similarly, the force-strain relationship, stiffness matrix and equivalent modulus of $[\pm 60]_5$ were derived in Eq. (3) to Eq. (5).

$$\begin{bmatrix} N_x \\ N_y \\ N_{xy} \end{bmatrix} = \begin{bmatrix} A_{11} & A_{12} & 0 \\ A_{12} & A_{22} & 0 \\ 0 & 0 & A_{66} \end{bmatrix} \begin{bmatrix} \varepsilon_x^0 \\ \varepsilon_y^0 \\ \gamma_{xy}^0 \end{bmatrix} + \begin{bmatrix} 0 & 0 & B_{16} \\ 0 & 0 & B_{26} \\ B_{16} & B_{26} & 0 \end{bmatrix} \begin{bmatrix} K_x \\ K_y \\ K_{xy} \end{bmatrix} \tag{3}$$

$$\begin{aligned} A_{11} &= 5t_0\left(\frac{1}{8}Q_{11} + \frac{3}{4}Q_{12} + \frac{3}{2}Q_{66} + \frac{9}{8}Q_{22}\right) \\ A_{12} &= 5t_0\left(\frac{3}{8}Q_{11} + \frac{3}{8}Q_{22} - \frac{3}{2}Q_{66} + \frac{5}{4}Q_{12}\right) \\ A_{22} &= 5t_0\left(\frac{9}{8}Q_{11} + \frac{3}{4}Q_{12} + \frac{3}{2}Q_{66} + \frac{1}{8}Q_{22}\right) \\ A_{66} &= 5t_0\left(\frac{3}{8}Q_{11} + \frac{3}{8}Q_{22} - \frac{3}{4}Q_{12} + \frac{1}{2}Q_{66}\right) \end{aligned} \tag{4}$$

$$E_{[\pm 60]x} = \frac{4\left(E_1{}^2v_{12}{}^2 + 3E_2G_{12}(v_{12}v_{21} - 1) - E_1(E_2 - 3G_{12}(1 + 2v_{12})(v_{12}v_{21} - 1))\right)}{(v_{12}v_{21} - 1)(6E_1v_{12} + 9E_1 + E_2 - 12G_{12}(v_{12}v_{21} - 1))} \tag{5}$$

3.2. Filling strategy: triangle

The deformation of each triangular element is symmetric along the geometric symmetry axis. Considering an element in Fig. 3a, subjected to the stress σ_0 in x direction, the balance of moment for beam AB gives

$$M = \frac{1}{2}P_{B1}\cos\theta l_1 \tag{6}$$

where P_{B1} is the force applied on beam AB. According to the standard beam theory, the deflection of beam AB can be written

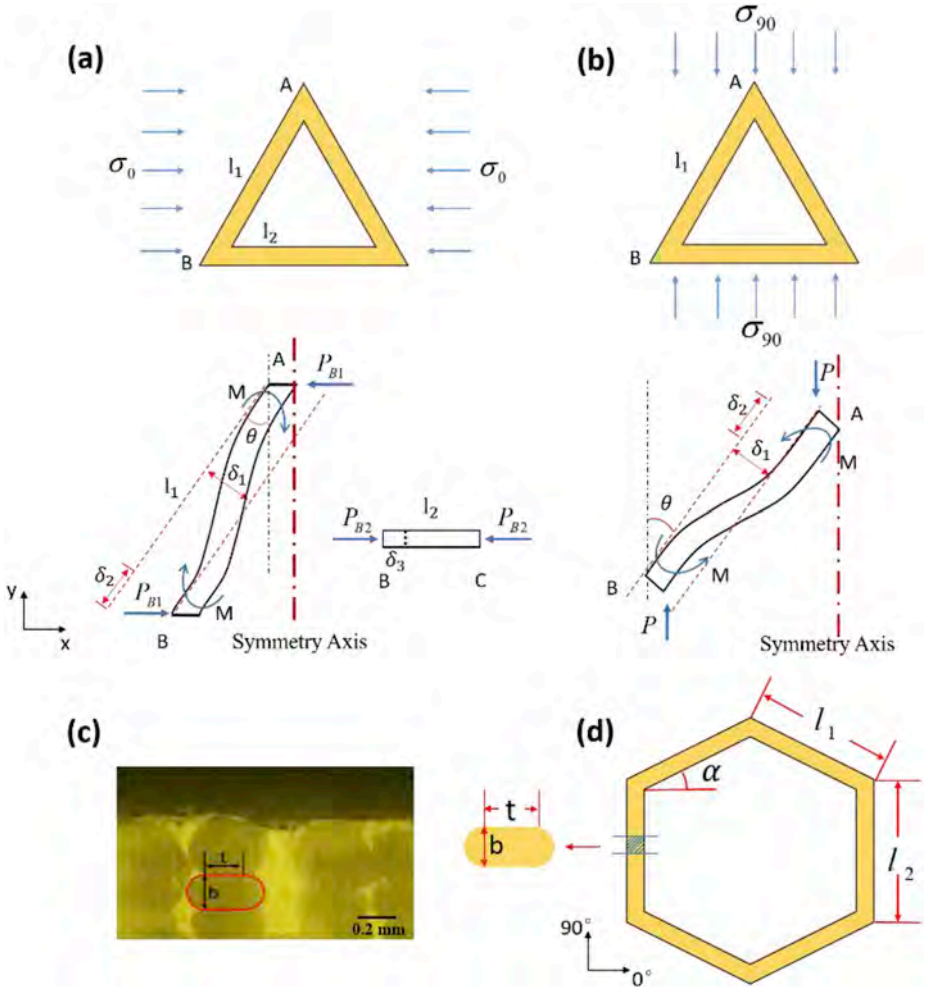

Fig. 3. Triangular element deformation under (a) loading in the [0] direction (b) loading in the [90] direction. (c) Optical image and geometry of the cross section of printed multilayer structure. (d) Hexagonal element of a two-dimensional model of printed structure.

$$\delta_1 = \frac{P_{B1} cos\theta l_1^3}{12 E_m I} \tag{7}$$

where*I*is the moment of inertia, E_m is the modulus of PLA filament. Based on the observation and measurement via microscope in Fig. 3c, the cross-section of printed filament is assumed to be a racetrack shape showing a rectangle in the middle and two semicircles on both sides with the height of b and width of t in straight line part. In this way, inter-bead voids, which are inherent to FDM and have a significant effect on the properties of printed components, are assumed to be the pores between adjacent ideal racetrack-shape filaments. From the parallel axis theorem, the moment of inertia is expressed as

$$I = \frac{bt^3}{12} + 2\left[0.00686b^4 + \frac{\pi b^2}{8}\left(\frac{t}{2} + \frac{2b}{3\pi}\right)^2\right] \tag{8}$$

The axial deformation of beam AB is

$$\delta_2 = \frac{P_{B1} sin\theta l_1}{E_m A} \tag{9}$$

where $A = \left(bt + \frac{1}{4}\pi b^2\right)$ is the cross-section area.

The axial deformation of beam BC is

$$\delta_3 = \frac{P_{B2} l_2}{E_m A} \tag{10}$$

where P_{B2} is the force applied on beam BC.

So, the effective strain in x direction is described as

$$\varepsilon_x = (\delta_1 cos\theta + \delta_2 sin\theta) / l_2 \tag{11}$$

According to the deformation compatibility condition $\delta_1 cos\theta + \delta_2 sin\theta = \delta_3$, we can obtain

$$P_{B2} = \frac{P_{B1}\left(Acos^2\theta {l_1}^3 + 12 I l_1 sin^2\theta\right)}{12 I l_2} \tag{12}$$

$$\sigma_x = \sigma_0 = (P_{B1} + P_{B2}) / (l_1 cos\theta b) \tag{13}$$

with Eq. (11) and Eq. (13), the equivalent modulus in x direction is

$$E_x = E_0 = \frac{\sigma_x}{\varepsilon_x} = \frac{A E_m\left(Acos^2\theta {l_1}^3 + 12 I(l_2 + l_1 sin^2\theta)\right)}{b cos\theta {l_1}^2\left(Acos^2\theta {l_1}^2 + 12 I sin^2\theta\right)} \tag{14}$$

Now considering the material properties in y direction in Fig. 3b, the triangular element is subjected to the stress σ_{90} in y direction, the balance condition gives

$$M = \frac{1}{2} P \sin\theta l_1 \tag{15}$$

where

$$P = \sigma_y b l_2 = \sigma_{90} b l_2 \tag{16}$$

Based on the beam theory, the beam AB deflects by

$$\delta_1 = \frac{P \sin\theta l_1^3}{12 E_m I} \tag{17}$$

The axial deformation of beam AB caused by force P is

$$\delta_2 = \frac{P \cos\theta l_1}{E_m A} \tag{18}$$

The strains in x and y direction are given in Eq. (19).

$$\begin{aligned} \varepsilon_x &= (\delta_2 \sin\theta - \delta_1 \cos\theta)/l_2 \\ \varepsilon_y &= (\delta_1 \sin\theta + \delta_2 \cos\theta)/l_1 \cos\theta \end{aligned} \tag{19}$$

The equivalent modulus in y direction is

$$E_y = E_{90} = \frac{\sigma_y}{\varepsilon_y} = \frac{12A \cos\theta E_m I}{12b \cos^2\theta I l_2 + A b {l_1}^2 l_2 \sin^2\theta} \tag{20}$$

3.3. Filling strategy: hexagon

Hexagonal structures are pervasively existed and applied in nature and various fields due to the superior properties of lightweight, high modulus ratio and flexible designability. The study of hexagonal honeycomb can be tracked back to several decades ago. Some representative researches include but not limited to Gibson et al. theory [47] based on Euler beam, Fu et al. theory [48] based on Timoshenko beam, and Evans et al. theory [49] involving the changes of angle between walls. Here the equivalent model of Fu. et al. is adopted according to the slenderness ratio of printed filament. By modifying the geometries and cross-section to racetrack like shape (Fig. 3d), equivalent modulus was derived in Eq. (21) with cross-section area $A = \left(bt + \frac{1}{4}\pi b^2\right)$ and moment of inertia I shown in Eq. (8).

$$\begin{aligned} E_0 &= \frac{12 A cos\alpha E m I}{b(l_2 + l_1 sin\alpha)\left(12 cos^2\alpha I + A {l_1}^2 sin^2\alpha\right)} \\ E_{90} &= \frac{12 A E m I(l_2 + l_1 sin\alpha)}{b cos\alpha {l_1}\left(A cos^2\alpha {l_1}^3 + 12 I\left(l_2 + l_1 sin^2\alpha\right)\right)} \end{aligned} \tag{21}$$

4. Results and discussion

4.1. Compressive behavior for cellular patterns

The morphologies of triangular and hexagonal cellular elements are shown in Fig. 4a and b. It's clear that uniformly distributed internal voids exist in cellular pattern structures, which will lead to lower densities when compared to straight-line structures. By calculating the lengths and density of filaments, the structural density ratio between

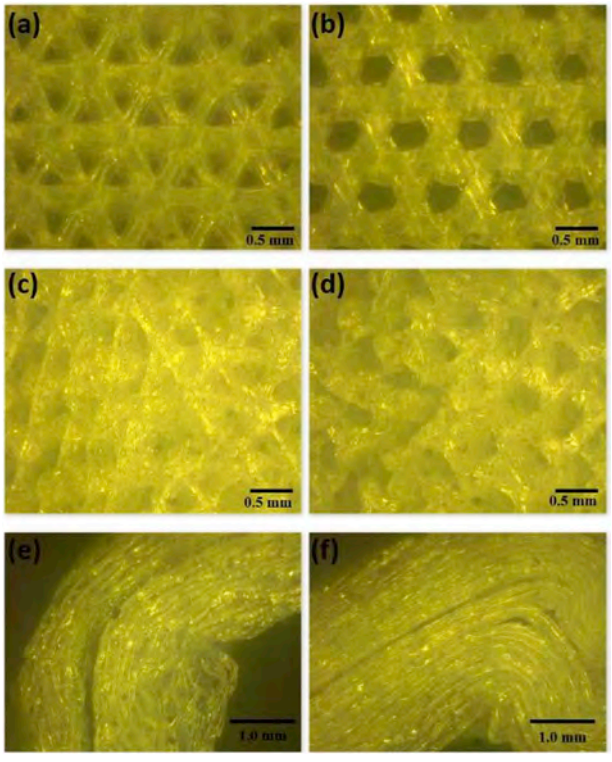

Fig. 4. Optical images of (a) triangular and (b) hexagonal elements before compression, (c) triangular and (d) hexagonal elements after compression, (e) triangular and (f) hexagonal side surfaces after compression.

straight-line structures and cellular structures was found to be 1.02 to 1.0.

Geometric parameters of different printed patterns that are used for the calculation of effective modulus are measured via KEYENCE VHX-900 microscope. The height (b) and width (t) of printed filament are measured on the cross section (Fig. 3c). The triangle and hexagon paths are both assumed to be regular. Table 2 compiles the average results of five-time measurements of different elements for each parameter.

Fig. 4c and d presents the optical images of triangular and hexagonal in-plane patterns after compression. It can be seen that the cellular elements become shriveled and the walls are invaginated under compressive loading, which indicate an advantage of energy absorption for printed structures with cellular patterns. Combining the flexible design of 3D printing, it's potential to achieve various structures that are capable of meeting different requirements and absorbing energy in practical application. The cross-section area of triangle (e) and hexagon (f) paths in fracture regions are displayed in Fig. 4e and f. Obvious delamination between printed layers and wrinkles of side layers can be observed. Even though visible delamination locates in the central area of thickness direction, the fractures of layers start from two sides and spread gradually to middle area.

The compression force-displacement curves in Fig. 5a show different stiffness and strength characteristics of triangle and hexagon patterns. To be specific, both [0] and [90] hexagon printing patterns have higher compressive strength than triangle elements. All cellular elements represent the gradual failure phenomenon instead of brittle failure after the peak point under compressive force, which can also verify the capability of energy absorption. It's obvious that the larger area under force-displacement curve is, the more energy that the structure can absorb.

4.2. Tensile properties of different printing patterns

Fig. 5b shows the force-displacement relation of filaments under uniaxial tension. It can be observed that the increments of force are nearly proportional to displacement before breaking, illustrating the elastic brittle characteristics of filaments. The modulus (E_m) and ultimate strain are 627.07 MPa and 3.63%, respectively. The tensile force-displacement curves of different filling patterns are demonstrated in Fig. 5c. For straight-line pattern structures, structure with [90] filling path possesses the highest modulus and strength, which are 1.32 and 1.72 times more than those of the lowest structure [0]. According to the results, we can conclude that the adhesive strength between printed filaments is relatively low, when compared to the strength of filament itself, providing evidence for the equivalent theory of straight-line patterns. Structures [±45] have the largest ultimate strain, and the largest elongation of deformation correspondingly. From this point of view, the mechanical performances of printed structures with straight line filling patterns are similar to the fiber woven reinforcement laminates. It's obvious that both triangle and hexagon elements have lower modulus and strength than straight-line patterns, the main reason behind which is that the interior voids of polygon elements induce lower actual density than straight-line filled structures. The load redistribution induced by the microstructures and the adhesion differences between filaments could also be potential reasons when all the specimens share the same actual density. Here, to evaluate the mechanical properties, we define the reduced modulus E_R as the ratio between modulus and mass ratio in Eq. (22) to eliminate weight effects.

$$E_R = \frac{E}{m} \tag{22}$$

where E is the equivalent modulus of printed structure, and m is the corresponding mass ratio (1.02:1). It means that m equals to 1.02 for straight-line specimens and 1.00 for cellular specimens. The normalized modulus is then defined by the ratio of the reduced modulus E_R to the modulus of filament E_m.

$$E_R^* = \frac{E_R}{E_m} \tag{23}$$

The comparisons of normalized modulus between experimental and theoretic data are shown in Fig. 5d. The data were also summarized in Table 3. We can see that the equivalent theories provide valid predictions of the effective modulus within a certain error range. The relative errors between modified classical laminate theory and experiments for straight-line patterns [0/90] and [±60] are 7.43% and 10.21%. Besides the printing accuracy and experiment errors, the assumptions that the equivalent relations along and perpendicular to printed filaments are taken as fiber and matrix also bring error to some extent. For the cellular elements, the relative errors for triangle [0], [90] and hexagon [0], [90] are 11.34%, 40.14%, 20.20% and 9.50%, respectively. We see the melting of filaments at high temperature when printing leads to irregular inter-bead voids (shown in Fig. 3c) and dimensional instability in actual printed structure, which causes discrepancies with the inter-bead voids assumed in the prediction model (Section 3). These differences and the simplification of equivalent models including the neglect of shear effects and angle changes under external forces would potentially result in the errors between experiments and prediction.

Table 2
Geometric parameters of printed structures from optical images.

Parameter	Height of printed filament b (mm)	Width of printed filament t (mm)	Side length of triangle L_T (mm)	Side length of hexagon L_H (mm)
Value	0.195	0.200	0.640	0.472

4.3. The effect of filling patterns on viscoelasticity

4.3.1. Generalized Maxwell-Wiechert model

Mechanical models are presented in this section to describe the viscoelastic polymeric behavior. Spring and damper elements, which are for elastic and viscous behaviors, respectively, can be combined in a variety of arrangements to produce a simulated viscoelastic response. In order to fully demonstrate the viscoelastic behaviors of different printed structures, generalized Maxwell-Wiechert model is adopted by considering a series of Maxwell elements and a free spring in parallel shown in Fig. 6. The equilibrium and kinematic equations are:

$$\begin{aligned} \sigma &= \sigma_1 + \sigma_2 + \cdots + \sigma_n + \sigma_\infty \\ \varepsilon &= \varepsilon_1 = \varepsilon_2 = \cdots = \varepsilon_n = \varepsilon_\infty \end{aligned} \tag{24}$$

where σ and ε are the total stress and strain. σ_i, ε_i and σ_∞, ε_∞ represent the stress and strain in Maxwell elements and free spring, respectively. n is the number of Maxwell elements.

For each Maxwell element, we have

$$\begin{aligned} \sigma_i &= \sigma_{\eta i} = \sigma_{Ei} \\ \varepsilon_i &= \varepsilon_{\eta i} + \varepsilon_{Ei} \end{aligned} \tag{25}$$

where $\sigma_{\eta i}$ and $\varepsilon_{\eta i}$ are the stress and strain for dashpot in the ith Maxwell element, and σ_{Ei} and ε_{Ei} are the stress and strain for spring in the ith Maxwell element. Combining Eq. (24) and Eq. (25), we can get the differential relation between the applied stress and strain as follows.

$$\begin{aligned} &\sigma + \left(\sum_{i=1}^{n}\frac{\eta_i}{E_i}\right)\dot{\sigma} + \frac{\eta_1\eta_2\cdots\eta_n}{E_1E_2\cdots E_n}\ddot{\sigma} + \cdots \\ &= E_\infty\varepsilon + \left[\sum_{i=1}^{n}\eta_i + E_\infty\left(\sum_{i=1}^{n}\frac{\eta_i}{E_i}\right)\right]\dot{\varepsilon} + \left(\sum_{i=1}^{n}\frac{\eta_1\eta_2\cdots\eta_n}{E_i} + E_\infty\frac{\eta_1\eta_2\cdots\eta_n}{E_1E_2\cdots E_n}\right)\ddot{\varepsilon} + \cdots \end{aligned} \tag{26}$$

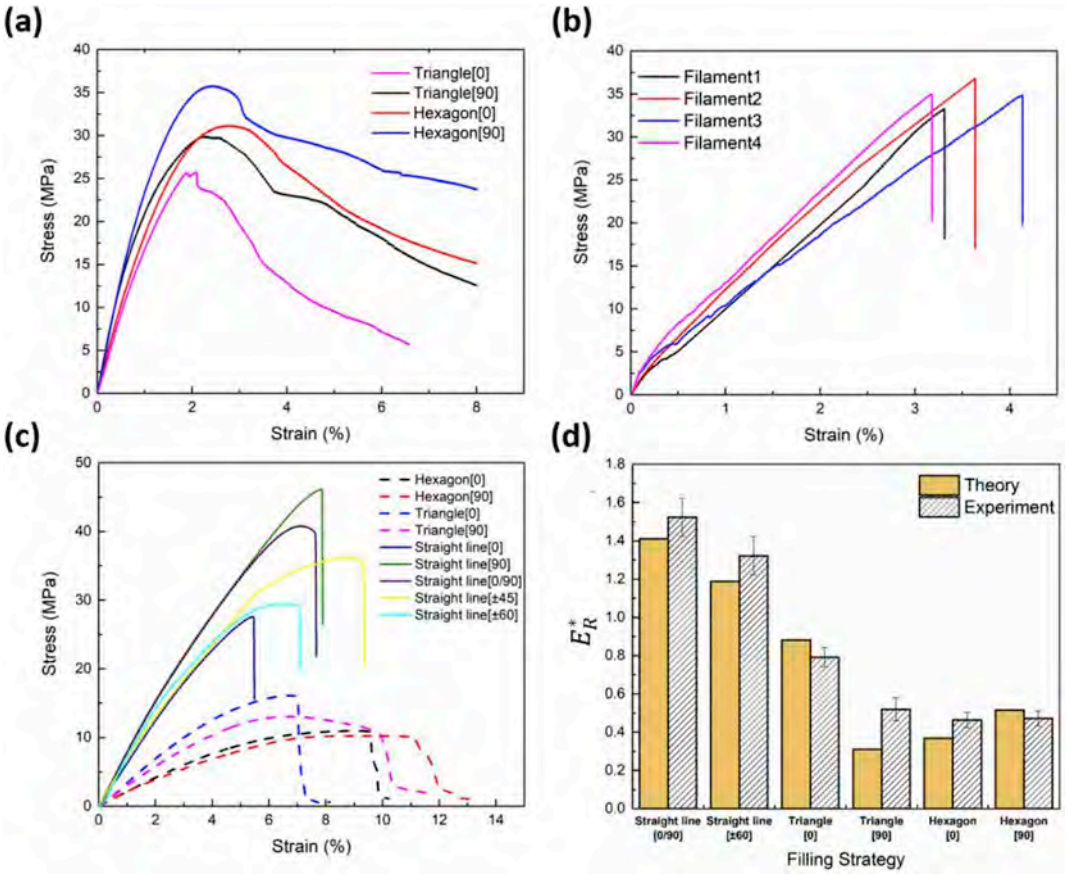

Fig. 5. Mechanical properties of different printing patterns. (a) Compressive stress-strain curves of cellular elements filled structures. (b) Tensile stress-strain curves of single filament. (c) Tensile stress-strain curves of straight line and cellular elements filled structures. (d) Comparison of the normalized modulus from experimental data and theoretic prediction. $E_R^* = (structural\ modulus\ /filament\ modulus)/mass\ ratio$.

Table 3
Result summarization of experiments and predictions.

Parameters		Value
Filament	Modulus	627.07 MPa
	Ultimate strain	3.63%
Relative errors between experiments and prediction	Straight-line pattern [0/90]	7.43%
	Straight-line pattern [±60]	10.21%
	Triangle [0]	11.34%
	Triangle [90]	40.14%
	Hexagon [0]	20.20%
	Hexagon [90]	9.50%

Rearranging Eq. (26) into

$$\sum_{i=0}^{n} K_i \frac{d^i\sigma}{dt^i} = \sum_{i=0}^{n} L_i \frac{d^i\varepsilon}{dt^i}$$

$$K_0 = 1, K_1 = \sum_{i=1}^{n} \frac{\eta_i}{E_i}, K_2 = \frac{\eta_1\eta_2\cdots\eta_n}{E_1E_2\cdots E_n}, \cdots$$

$$L_0 = E_\infty, L_1 = \sum_{i=1}^{n} \eta_i + E_\infty\left(\sum_{i=1}^{n} \frac{\eta_i}{E_i}\right), L_2 = \sum_{i=1}^{n} \frac{\eta_1\eta_2\cdots\eta_n}{E_i} + E_\infty \frac{\eta_1\eta_2\cdots\eta_n}{E_1E_2\cdots E_n}, \cdots \quad (27)$$

Assuming that the model is subjected to a step increase in strain, represented in Eq. (28), during the relaxation process at constant strain. $H(t)$ is the Heaviside step function. Solution of Eq. (27) gives the time dependent stress in Eq. (29), where the time dependent modulus is shown in Eq. (30). It can be seen that the initial modulus (E_0) without relaxation is $E_\infty + \sum_{i=1}^{n} E_i$, while the long-term modulus is E_∞ after full relaxation.

$$\varepsilon = \varepsilon_0 H(t) \quad (28)$$

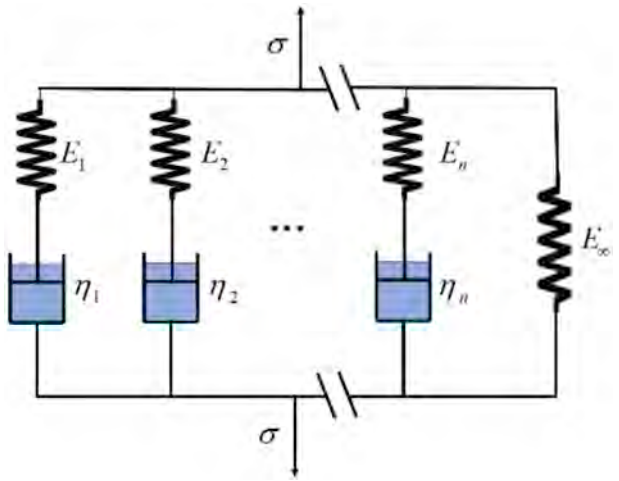

Fig. 6. Generalized Maxwell-Wiechert model with n Maxwell elements and a free spring in parallel.

$$\sigma(t) = \varepsilon_0 E(t) \tag{29}$$

$$E(t) = E_\infty + \sum_{i=1}^{n} E_i e^{-\frac{t}{\tau_i}}, \tau_i = \frac{\eta_i}{E_i} \tag{30}$$

The dimensionless modulus g(t) can be defined as the ratio of relaxation modulus to the initial modulus in Eq. (31), which is the representation of Prony series. g(t) varies from initial value g (0) = 1 to long-term value $g(\infty) = 1 - \sum_{i=1}^{n} g_i$. The value g_i indicates the potential relaxation fraction of the material at the timescale τ_i.

$$g(t) = 1 - \sum_{i=1}^{n} g_i \left(1 - e^{-\frac{t}{\tau_i}}\right)$$
$$g_i = \frac{E_i}{E_0}, E_0 = E_\infty + \sum_{i=1}^{n} E_i \tag{31}$$

4.3.2. Descriptions for different patterns

The relationships between relaxation modulus and time at 65 °C from relaxation tests are shown in Fig. 7. The modulus decreases sharply with time at the initial stage and gradually reaches the steady value as time approaches infinity. We see that specimens with hexagon [90] pattern still show evident relaxation at the observation time of 1200s. Generalized Maxwell-Wiechert models are fitted to the relaxation data by using least squares approach. Six relaxation timescales (τ_i) were selected from 0.01s to 1000s to improve the fitting accuracy (R-Square≥97.8%). The equations (Eq.(S17)) of time dependent modulus for different printed structures are listed in Supplementary Information (SI) section S3. Table 4 gives the dimensionless modulus and relaxation timescales. It can be observed that straight-line [0/90] pattern possesses the minimum fractional decrease of modulus 59.213% after a long-term relaxation. Cellular patterns show higher fractional decreases than straight-line patterns due to the existence of interior voids. During the fitting process, the coefficient g_i of some timescale becomes zero, meaning that there is no obvious relaxation at this timescale. Consequently, it can be seen that no apparent stress relaxation would occur at the timescale of 0.1s for all six types of patterns. In addition, the relaxations were not observed at the timescale of 0.01s for patterns of straight line [±60], triangle [0] and triangle [90]. A comprehensive understanding of relaxation timescales and the corresponding fractional decreases of modulus for different printing patterns is conducive to the selection of printing strategy.

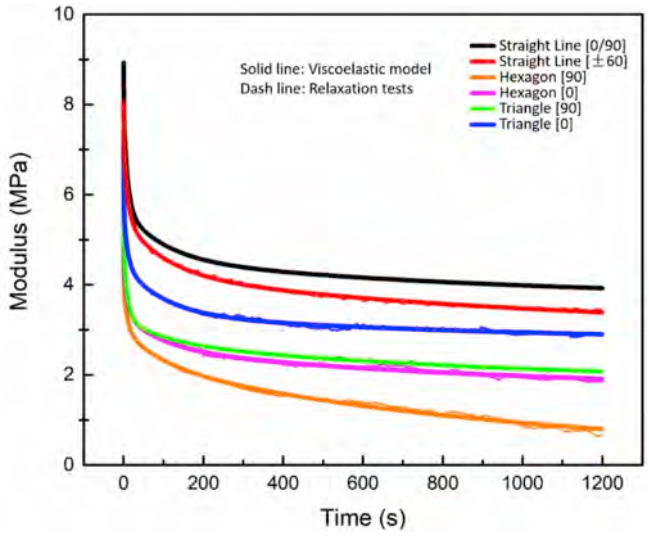

Fig. 7. Relaxation test curves and viscoelastic model fitting curves of printed structures with different patterns (Solid line: viscoelastic model prediction. Dash line: relaxation tests.).

Table 4
The dimensionless modulus and relaxation timescale.

	Straight line [0/90]	Straight line [±60]	Hexagon [90]	Hexagon [0]	Triangle [90]	Triangle [0]
	8.92683	8.03693	4.7832	5.8446	6.48337	7.38446
	0.59213	0.62597	0.96449	0.72258	0.72382	0.63328
g_1	0.04780	0.09992	0.02369	0.00501	0.26673	0.24139
g_2	0.10166	0.21804	0.16077	0.24026	0.22679	0.15564
g_3	0.23758	0.15049	0.18900	0.18244	0.08443	0.15063
g_4	0.12488	0.15751	0.15566	0.13125	0.14587	0.08562
g_5	0.10467	/	0.43537	0.16363	/	/
	0.01	1	0.01	0.01	1	1
	1	10	1	1	10	10
	10	100	10	10	100	100
	100	1000	100	100	1000	1000
	1000	/	1000	1000	/	/

4.4. Shape memory properties and a 3D demonstration

4.4.1. Shape memory properties

Fig.S2 illustrates the recovery angle and temperature changes with time for different printing patterns. In the period of 0s–400s, the printed specimens are deformed 180° to U type at glass transition temperature followed by the temperature decrease (400s–580s) under the maintaining of external force. It's found that the external forces needed for the deformation of specimens with straight line [0] are the smallest, the reason behind which is that the internal forces of bending straight line [0] are mostly from the adhesion between printed filaments. Then, the specimens are placed at room temperature without external force in 580s–1180s. For the recovery process beginning at 1180s, it's observed that specimens with crossed printing angles ([±45] and [±60]) need more time to recover to its final state when compared to other printing patterns, especially between which specimens [±45] have the longest recovery time of around 80s. While specimens with other seven kinds of printing patterns complete the recovery process within 40s. Overall, printed specimens despite of the filling patterns possess relatively fast recovery speed in the middle stage of recovery due to the adequate heat and stored strain energy. To evaluate the shape recovery capacity, here the recovery ratio is defined as Recovery ratio = $(1 - \textit{final recovery angle}/180) \times 100\%$. We can see that the recovery ratios of specimens with straight line [0] are the lowest in all kinds of specimens and decrease when temperature increases from 55 °C to 65 °C in Fig. 8. The reason is that the stiffness along printed filaments (straight line [90]) is larger than that in transverse direction (straight line [0]) (Fig. 5c), which leads to lower recovery force of straight line [0] that cannot overcome the water resistance. In the short recovery period, the water absorption of printed PLA components was negligible to focus on the pattern effects. As a result, residual angle is generated in the competition of recovery force and water resistance. According to the typical Dynamic Mechanical Analysis (DMA) curves of SMP, modulus decrease dramatically in the vicinity of Tg, which corresponds to the reduction of recovery force in higher temperature. An effective way to improve the recovery ratio is to conduct the recovery process under the condition of less resistance, such as in the air. The shape fixity ratios stabilized in the range of 99.72%–100% after 50min and remained unchanged during the test observation time of 1200min.

4.4.2. A 2D and 3D convertible structure with programmable Poisson's ratio

To demonstrate the potential functional application of the 4D printed shape memory PLA, a 2D and 3D convertible structure with programmable Poisson's ratio is fabricated via FDM technique shown in Fig. 9. Based on the analyzation above, straight-line pattern with angle of [±45], which has good elongation before break, is selected for printing.

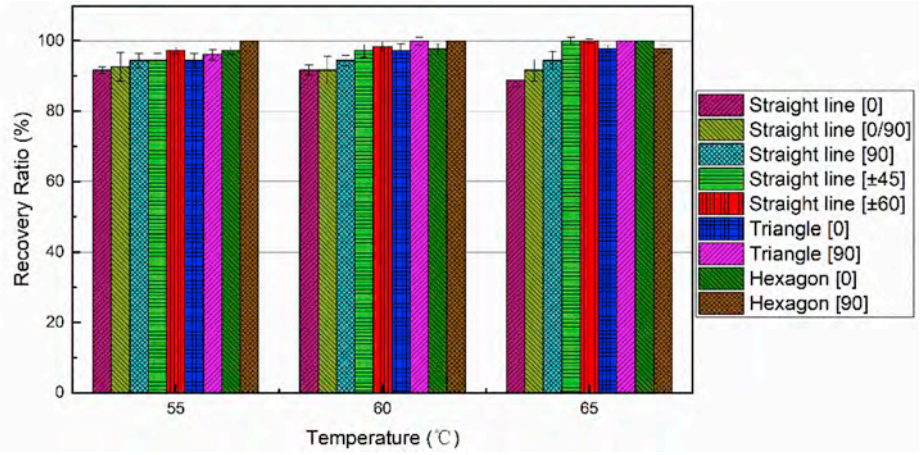

Fig. 8. Shape recovery ratios of designed printing patterns in the vicinity of Tg.

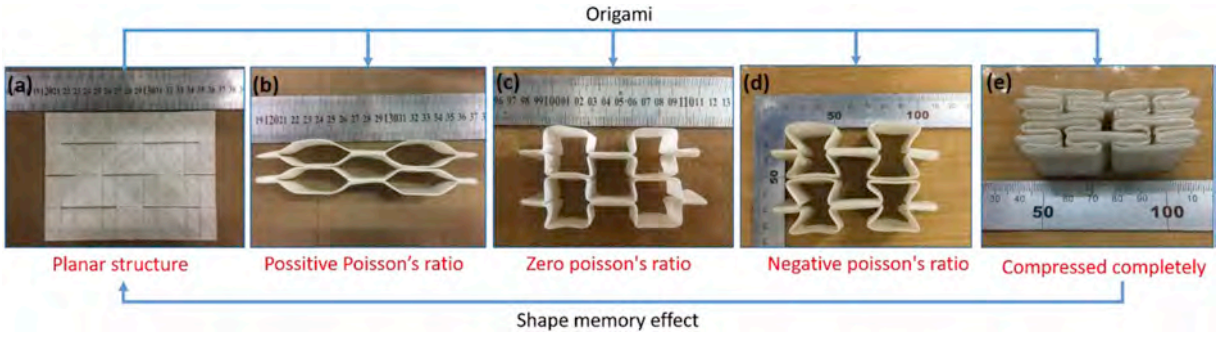

Fig. 9. Demonstration of 2D and 3D convertible structure with programmable Poisson's ratio.

Firstly, a planar structure is printed with predesigned creases in Fig. 9a, then molded to different multifunctional 3D structures with positive (Fig. 9b), zero (Fig. 9c) and negative (Fig. 9d) Poisson's ratio according to different requirements. This 2D to 3D process is operated with the combination of origami at 60 °C and cooled down to room temperature to fix the deformed shape. The completely compressive state of the 3D structure is shown in Fig. 9e. The longitudinal and lateral contraction ratios between the fully compressive state and the original planar state are approximately 40% and 18%, providing considerable portability for practical application. From Fig. 9e–a, the deformed 3D structure has the capability of recovering to its original 2D shape when heated to the temperature in the vicinity of Tg due to shape memory effect.

We can expect controllable stiffness of the 3D structure under different temperatures and shapes on account of the varying modulus of shape memory PLA with temperature. The designability and functionality are also reflected in the programmable Poisson' ratio and contraction ratio by adjusting the length ratio of adjacent edges and the number of elements. More experimental evaluations of the convertible structure will be included in further developments.

5. Conclusion

In this paper, nine kinds of specimens with infill patterns of straight line and polygon are fabricated by FDM to explore the anisotropic performance and compared with prediction theories. As a result, we see that triangular and hexagonal elements have lower effective modulus and strength than straight-line patterns because of the interior voids of cellular elements. The prediction theories for straight-line and polygonal patterns are developed based on classical laminate theory and honeycomb equivalent modulus theory, respectively, showing a good agreement with experimental results within reasonable error range. Polygonal pattern printed structures show the superiority of energy absorption under compressive loading, which make it possible to design various energy absorbing devices without the geometrical limitation of 3D printing. The viscoelasticity differences between patterns are described by generalized Maxwell-Wiechert model and fitted by Prony series using relaxation test data. For shape memory properties, all printed specimens exhibit the shape recovery ratio of over 91% with the existence of water resistance and shape fixity ratio of over 99.72% after 20 h under room temperature. The contraction ratios of the 2D and 3D convertible structure with 5 elements in longitudinal and lateral direction can reach 40% and 18%, which are adjustable by changing the length ratio and element number. This study will help understand the effect of 4D printing microarchitecture and shed light on its multifunctional development.

Acknowledgement

This work is supported by the National Natural Science Foundation of China (Grant Nos. 11632005 and 11672086) and the Foundation for Innovative Research Groups of the National Natural Science Foundation of China (Grant No. 11421091).

Appendix A. Supplementary data

Supplementary data to this article can be found online at https://doi.org/10.1016/j.compscitech.2019.107935.

References

[1] Y. Bao, Y. Han, L. Yang, N. Li, J. Luo, W. Qu, R. Chen, A.K.Y. Jen, T. Li, H. Chen, Bioinspired controllable electro-chemomechanical coloration films, Adv. Funct. Mater. 29 (2) (2019), 1806383.
[2] J.L. Katz, Anisotropy of Young's modulus of bone, Nature 283 (5742) (1980) 106.
[3] C. Brookes, R. Burnand, J. Morgan, Anisotropy and indentation creep in crystals with the rocksalt structure, J. Mater. Sci. 10 (12) (1975) 2171–2173.
[4] C.H. Chen, A.R. Abate, D. Lee, E.M. Terentjev, D.A. Weitz, Microfluidic assembly of magnetic hydrogel particles with uniformly anisotropic structure, Adv. mater. 21 (31) (2009) 3201–3204.
[5] W. Yang, H. Furukawa, J.P. Gong, Highly extensible double-network gels with self-assembling anisotropic structure, Adv. Mater. 20 (23) (2008) 4499–4503.
[6] P. Xu, T. Liu, S. Pan, Z. Zhou, Numerical analysis for micro-vibration isolation of jointed sandwich plates with mass blocks, Mater. Today. Commun. 17 (2018) 341–354.
[7] L.-C. Wang, W.-L. Song, D. Fang, Twistable origami and kirigami: from structure-guided smartness to mechanical energy storage, ACS Appl. Mater. Interfaces 11 (3) (2018) 3450–3458.
[8] J. Chen, X. Yuan, M. Chen, X. Cheng, A. Zhang, G. Peng, W.-L. Song, D. Fang, Ultrabroadband three-dimensional printed radial perfectly symmetric gradient honeycomb all-dielectric dual-directional lightweight planar luneburg lens, ACS Appl. Mater. Interfaces 10 (44) (2018) 38404–38409.
[9] H. Lipson, M. Kurman, Fabricated: the New World of 3D Printing, John Wiley & Sons, 2013.
[10] J.T. Muth, D.M. Vogt, R.L. Truby, Y. Mengüç, D.B. Kolesky, R.J. Wood, J.A. Lewis, Embedded 3D printing of strain sensors within highly stretchable elastomers, Adv. Mater. 26 (36) (2014) 6307–6312.
[11] A. Suiker, Mechanical performance of wall structures in 3D printing processes: theory, design tools and experiments, Int. J. Mech. Sci. 137 (2018) 145–170.
[12] M. Khan, S. Kumar, Performance enhancement of tubular multilayers via compliance-tailoring: 3D printing, testing and modeling, Int. J. Mech. Sci. 140 (2018) 93–108.
[13] Y. Mao, Z. Ding, C. Yuan, S. Ai, M. Isakov, J. Wu, T. Wang, M.L. Dunn, H.J. Qi, 3D printed reversible shape changing components with stimuli responsive materials, Sci. Rep. 6 (2016) 24761.
[14] Z. Zhang, K.G. Demir, G.X. Gu, Developments in 4D-printing: a review on current smart materials, technologies, and applications, Int. J. Soc. Netw. Min. (2019) 1–20.
[15] S. Kumar, B.L. Wardle, M.F. Arif, J. Ubaid, Stress reduction of 3D printed compliance-tailored multilayers, Adv. Eng. Mater. 20 (1) (2018) 1700883.
[16] B.G. Compton, J.A. Lewis, 3D-printing of lightweight cellular composites, Adv. mater. 26 (34) (2014) 5930–5935.
[17] S. Tibbits, 4D printing: multi-material shape change, Architect. Des 84 (1) (2014) 116–121.
[18] F. Momeni, X. Liu, J. Ni, A review of 4D printing, Mater. Des. 122 (2017) 42–79.
[19] Q. Ge, H.J. Qi, M.L. Dunn, Active materials by four-dimension printing, Appl. Phys. Lett. 103 (13) (2013), 131901.
[20] A.R. Rajkumar, K. Shanmugam, Additive manufacturing-enabled shape transformations via FFF 4D printing, J. Mater. Res. 33 (24) (2018) 4362–4376.
[21] A.S. Gladman, E.A. Matsumoto, R.G. Nuzzo, L. Mahadevan, J.A. Lewis, Biomimetic 4D printing, Nat. Mater. 15 (4) (2016) 413.
[22] Y. Zhou, W.M. Huang, S.F. Kang, X.L. Wu, H.B. Lu, J. Fu, H. Cui, From 3D to 4D printing: approaches and typical applications, J. Mech. Sci. Technol. 29 (10) (2015) 4281–4288.
[23] J. Choi, O.-C. Kwon, W. Jo, H.J. Lee, M.-W. Moon, 4D printing technology: a review, 3D Print. Addit. Manuf. 2 (4) (2015) 159–167.
[24] T. Liu, T. Zhou, Y. Yao, F. Zhang, L. Liu, Y. Liu, J. Leng, Stimulus methods of multi-functional shape memory polymer nanocomposites: a review, Compos. Appl. Sci. Manuf. 100 (2017) 20–30.
[25] T. Mu, L. Liu, X. Lan, Y. Liu, J. Leng, Shape memory polymers for composites, Compos. Sci. Technol. 160 (2018) 169–198.
[26] X. Lan, Y. Liu, H. Lv, X. Wang, J. Leng, S. Du, Fiber reinforced shape-memory polymer composite and its application in a deployable hinge, Smart Mater. Struct. 18 (2) (2009), 024002.
[27] Q. Ge, C.K. Dunn, H.J. Qi, M.L. Dunn, Active origami by 4D printing, Smart Mater. Struct. 23 (9) (2014), 094007.
[28] A. Lendlein, H. Jiang, O. Jünger, R. Langer, Light-induced shape-memory polymers, Nature 434 (7035) (2005) 879.
[29] R. Mohr, K. Kratz, T. Weigel, M. Lucka-Gabor, M. Moneke, A. Lendlein, Initiation of shape-memory effect by inductive heating of magnetic nanoparticles in thermoplastic polymers, Proc. Natl. Acad. Sci. 103 (10) (2006) 3540–3545.
[30] Y. Liu, H. Lv, X. Lan, J. Leng, S. Du, Review of electro-active shape-memory polymer composite, Compos. Sci. Technol. 69 (13) (2009) 2064–2068.
[31] W. Huang, B. Yang, L. An, C. Li, Y. Chan, Water-driven programmable polyurethane shape memory polymer: demonstration and mechanism, Appl. Phys. Lett. 86 (11) (2005), 114105.
[32] Q. Ge, A.H. Sakhaei, H. Lee, C.K. Dunn, N.X. Fang, M.L. Dunn, Multimaterial 4D printing with tailorable shape memory polymers, Sci. Rep. 6 (2016), 31110.
[33] M. Bodaghi, A. Damanpack, W. Liao, Self-expanding/shrinking structures by 4D printing, Smart Mater. Struct. 25 (10) (2016), 105034.
[34] B. Gao, Q. Yang, X. Zhao, G. Jin, Y. Ma, F. Xu, 4D bioprinting for biomedical applications, Trends Biotechnol. 34 (9) (2016) 746–756.
[35] X. Kuang, K. Chen, C.K. Dunn, J. Wu, V.C. Li, H.J. Qi, 3D printing of highly stretchable, shape-memory, and self-healing elastomer toward novel 4D printing, ACS Appl. Mater. Interfaces 10 (8) (2018) 7381–7388.
[36] K.-L. Zhang, X.-D. Cheng, Y.-J. Zhang, M. Chen, H. Chen, Y. Yang, W.-L. Song, D. Fang, Weather-manipulated smart broadband electromagnetic metamaterials, ACS Appl. Mater. Interfaces 10 (47) (2018) 40815–40823.
[37] S.E. Bakarich, R. Gorkin III, M.I.H. Panhuis, G.M. Spinks, 4D printing with mechanically robust, thermally actuating hydrogels, Macromol. Rapid Commun. 36 (12) (2015) 1211–1217.
[38] M. Vaezi, C.K. Chua, Effects of layer thickness and binder saturation level parameters on 3D printing process, Int. J. Adv. Manuf. Technol. 53 (1–4) (2011) 275–284.
[39] S. Belhabib, S. Guessasma, Compression performance of hollow structures: from topology optimisation to design 3D printing, Int. J. Mech. Sci. 133 (2017) 728–739.
[40] R. Gautam, S. Idapalapati, S. Feih, Printing and characterisation of Kagome lattice structures by fused deposition modelling, Mater. Des. 137 (2018) 266–275.
[41] J. Yin, C. Lu, J. Fu, Y. Huang, Y. Zheng, Interfacial bonding during multi-material fused deposition modeling (FDM) process due to inter-molecular diffusion, Mater. Des. 150 (2018) 104–112.
[42] C. Lubombo, M.A. Huneault, Effect of infill patterns on the mechanical performance of lightweight 3D-printed cellular PLA parts, Mater. Today. Commun. 17 (2018) 214–228.
[43] C.R. Garcia, J. Correa, D. Espalin, J.H. Barton, R.C. Rumpf, R. Wicker, V. Gonzalez, 3D printing of anisotropic metamaterials, Prog. Electromagn. Res. 34 (2012) 75–82.
[44] C. Casavola, A. Cazzato, V. Moramarco, C. Pappalettere, Orthotropic mechanical properties of fused deposition modelling parts described by classical laminate theory, Mater. Des. 90 (2016) 453–458.
[45] D. Croccolo, M. De Agostinis, G. Olmi, Experimental characterization and analytical modelling of the mechanical behaviour of fused deposition processed parts made of ABS-M30, Comput. Mater. Sci. 79 (2013) 506–518.
[46] W. Zhang, F. Zhang, X. Lan, J. Leng, A.S. Wu, T.M. Bryson, C. Cotton, B. Gu, B. Sun, T.-W. Chou, Shape memory behavior and recovery force of 4D printed textile functional composites, Compos. Sci. Technol. 160 (2018) 224–230.
[47] L.J. Gibson, M.F. Ashby, G. Schajer, C. Robertson, The mechanics of two-dimensional cellular materials, Proc. R. Soc. A Math. Phys. Sci. 382 (1782) (1982) 25–42.
[48] F. Minghui, Y. Jiuren, Equivalent elastic parameters of the honeycomb core, Acta Mech. Sin. 31 (1) (1999) 113–118.
[49] I. Masters, K. Evans, Models for the elastic deformation of honeycombs, Compos. Struct. 35 (4) (1996) 403–422.